First-principles mode-by-mode analysis for electron-phonon scattering channels and mean free path spectra in GaAs

Te-Huan Liu,[1] Jiawei Zhou,[1] Bolin Liao,[1] David J. Singh,[2] and Gang Chen[1,*]

[1]*Department of Mechanical Engineering, Massachusetts Institute of Technology, Cambridge, Massachusetts 02139, USA*

[2]*Department of Physics and Astronomy, University of Missouri, Columbia, Missouri 65211, USA*

(Received 11 May 2016; revised manuscript received 20 January 2017; published 16 February 2017)

We present a first-principles framework to investigate the electron scattering channels and transport properties for polar materials by combining the exact solution of the linearized electron-phonon (e-ph) Boltzmann transport equation in its integral-differential form associated with the e-ph coupling matrices obtained from the polar Wannier interpolation scheme. No *ad hoc* parameter is required throughout this calculation, and GaAs, a well-studied polar material, is used as an example to demonstrate this method. In this work, the long-range and short-range contributions as well as the intravalley and intervalley transitions in the e-ph interactions (EPIs) have been quantitatively addressed. Promoted by such mode-by-mode analysis, we find that in GaAs, the piezoelectric scattering is comparable to deformation-potential scattering for electron scatterings by acoustic phonons in EPI even at room temperature, and it makes a significant contribution to mobility. Furthermore, we achieved good agreement with experimental data for the mobility, and we identified that electrons with mean free paths between 130 and 210 nm provide the dominant contribution to the electron transport at 300 K. Such information provides a deeper understanding of the electron transport in GaAs, and the presented framework can be readily applied to other polar materials.

DOI: 10.1103/PhysRevB.95.075206

I. INTRODUCTION

Electron-phonon interaction (EPI) was first studied by Bloch [1] in 1928. Bloch discussed the interference between electrons and elastic waves and their effect on the temperature dependence of electrical conductivity. It was then realized that EPI was at the center of electron transport, as the key limiting factor of the carriers' lifetime in ordinary metals [2,3] and semiconductors [4–8] in a large temperature range, apart from its other roles in the hot-electron thermalization process [9,10], as well as in superconductivity [11,12]. The essence of EPI lies in the fact that, when the atoms move around due to thermal vibrations, the potential seen by electrons is disturbed. Such perturbation leads to exchange of energy and momentum between electrons and phonons, which then determines the electron lifetimes. Based on this picture, quasi-analytical forms of electron-phonon (e-ph) coupling matrices for different types of scattering mechanisms have been derived, and these have been employed to obtain scattering rates based on Fermi's golden rule, either analytically or computationally, which then can be used to explain electron transport properties [7,8]. Bardeen and Shockley [4] first proposed an insightful concept known as the deformation potential for EPI in semiconductors, which relates the strength of electron-acoustic-phonon interaction to the shift of the band edges due to local strain. Long-wavelength acoustic phonons generate a corresponding dilation in the crystal, and the relative changes in atomic spacing give rise to a perturbed potential that tends to shift the electronic band energy and thereby to couple with electrons. In this case, the perturbed potential is approximately proportional to strain, or $V_{\text{e-ph}} = \Xi_{\text{ADP}} \nabla \cdot \mathbf{u}$, where Ξ_{ADP} is the acoustic deformation potential, and $\mathbf{u}$ is the displacement of the atom. Herring and Vogt [5] generalized the deformation-potential theory and computed relaxation time tensors and mobilities of silicon and n-type germanium. Harrison [13] extended the deformation-potential theory to optical phonons that exist when each lattice point has two or more atoms as the basis. For long-wavelength optical phonons, the atoms vibrate against each other without changing the size of the unit cell, in contrast to acoustic phonons, and the variation of the distances between basis atoms directly disturbs the surrounding lattice potential, which acts as a scattering source to electrons. In this picture, the perturbed potential is nearly proportional to atomic displacement as $V_{\text{e-ph}} = \Xi_{\text{ODP}} u$ [14], where Ξ_{ODP} is the optical deformation potential.

The deformation potential describes only the short-range interactions between electrons and long-wavelength phonons. When polar materials are considered, the electric dipole field generated by charged atoms decays slowly. The long-range interactions cause additional scattering for electrons—the long-wavelength acoustic phonon induces lattice strain, which is called piezoelectric scattering, while the long-wavelength optical phonon induces bond stretching in the lattice, which is called polar-optical-phonon scattering. Meijer and Polder [15] first discussed the electron scattering by macroscopic piezoelectric fields, which is generated by lattice distortion when the inversion center is absent in a crystal. Their study revealed that the piezoelectric scattering predominates at very low temperatures. On the other hand, the longitudinal-optical (LO) phonon serves as a strong scattering source to electrons in polar materials due to the induced macroscopic polarization field, which was first investigated by Fröhlich [16]. If the dielectric screening is small, the direct effect of the dipole field can dominate, and so the polar-optical-phonon interaction is usually the major scattering channel in polar materials at room temperature. A good discussion on short-range and long-range EPIs is given by Vogl [17].

*Author to whom correspondence should be addressed: gchen2@mit.edu

 ©2017 American Physical Society

TABLE I. Semiempirical formulae for the e-ph coupling matrix and scattering rate of different EPIs [8,32]. The abbreviations stand for, sequentially, acoustic-deformation-potential, optical-deformation-potential, piezoelectric, and polar-optical-phonon scatterings. These formulae are used to indicate the dependency of the phonon wave vector $\mathbf{q}$ and electron energy $\varepsilon_{\mathbf{k}}$ of the coupling matrix and scattering rate, respectively. Here, e is the electron charge, m_e is the electron elective mass, Ω is the volume of the unit cell, and ρ is the mass density of the material. The terms $v_{\mathbf{q}}$, $\omega_{\mathbf{q}}$, and $n_{\mathbf{q}}^0$ are the phonon group velocity, frequency, and distribution function at the equilibrium state, respectively. The screening effect is shown by ϵ_∞ and ϵ_0, which are the high-frequency (no lattice response) and static (including lattice response) dielectric constants, respectively. In the piezoelectric application, e_{PZ} represents the first-order piezoelectric constant, and λ_{D} is the Debye screening length.

Mechanism	Coupling matrix $\mathbf{M_q}$	Scattering rate $\tau^{-1}(\varepsilon_{\mathbf{k}})$
ADP	$\sqrt{\frac{\Xi_{\mathrm{ADP}}^2 \hbar \lvert\mathbf{q}\rvert}{2\rho\Omega v_{\mathbf{q}}}}$	$\frac{\Xi_{\mathrm{ADP}}^2 (2m_e)^{3/2} k_{\mathrm{B}} T}{2\pi\hbar^3 \rho v_{\mathbf{q}}^2}\sqrt{\varepsilon_{\mathbf{k}}}$
ODP	$\sqrt{\frac{\Xi_{\mathrm{ODP}}^2 \hbar}{2\rho\Omega \omega_{\mathbf{q}}}}$	$\frac{\Xi_{\mathrm{ODP}}^2 (2m_e)^{3/2}}{4\pi\hbar^3 \rho \omega_{\mathbf{q}}}[(n_{\mathbf{q}}^0 + \frac{1}{2} \mp \frac{1}{2})\sqrt{\varepsilon_{\mathbf{k}} \pm \hbar\omega_{\mathbf{q}}}]$
PZ	$\sqrt{\frac{e_{\mathrm{PZ}}^2 \hbar}{2\rho\Omega v_{\mathbf{q}}}\frac{e^2}{\epsilon_\infty \lvert\mathbf{q}\rvert}}$	$\frac{e_{\mathrm{PZ}}^2 e^2 k_{\mathrm{B}} T}{\pi\hbar^2 \epsilon_\infty^2 \sqrt{2\varepsilon_{\mathbf{k}}/m_e}} \ln(1 + \frac{8 m_e \varepsilon_{\mathbf{k}}/\hbar^2}{\lambda_{\mathrm{D}}^2})$
POP	$\frac{ie}{\lvert\mathbf{q}\rvert}\sqrt{\frac{2\pi\hbar\omega_{\mathbf{q}}}{\Omega}(\frac{1}{\epsilon_\infty} - \frac{1}{\epsilon_0})}$	$\frac{e^2 \omega_{\mathbf{q}}(\frac{1}{\epsilon_\infty} - \frac{1}{\epsilon_0})}{2\pi\hbar\epsilon_\infty\sqrt{2\varepsilon_{\mathbf{k}}/m_e}}[(n_{\mathbf{q}}^0 + \frac{1}{2} \mp \frac{1}{2})\sinh^{-1}\sqrt{\frac{\varepsilon_{\mathrm{k}}}{\hbar\omega_{\mathbf{q}}} - \frac{1}{2} \pm \frac{1}{2}}]$

We summarize the semiempirical formulae of the e-ph coupling matrix as well as scattering rate for the four scattering mechanisms in Table I; for polar-optical-phonon interactions, the formula is usually referred to as the Fröhlich model, while for piezoelectric interactions, the formula is referred to as the Hutson model [18]. These phenomenological models are widely employed to study the electron transport properties in nonpolar materials through the Boltzmann transport equation (BTE) under relaxation time approximation (RTA) [5,10,13,18]. In polar semiconductors, however, the validity of the RTA is questionable owing to the strong inelastic scattering caused by LO phonons [7,8]. The variational principle [19–21], Rode's iterative scheme [22–28], as well as the Monte Carlo method [29–31] have been employed to extract the electron mobility of polar materials. However, these readily used semiempirical models have strong limitations to qualitatively investigating EPI mode-by-mode due to the simplifications made in the derivations. Models for the coupling matrices only depend on the magnitude of the phonon wave vectors; the periodic part of the Bloch function near the band edge, at which most transition events occur, is usually changed smoothly, and therefore the overlap integral can be taken to be unity to take away the dependence of electron state [32]. This dependency restricts the applicability of such models to only isotropic crystals. The Debye model is used for acoustic phonons to describe the linear dispersion behavior at the long-wavelength limit, while the dispersionless assumption is made for optical phonons. Furthermore, the parabolic band assumption is implemented to achieve the explicit formulae for electron scattering rates. To facilitate the understanding of materials and promote the discovery of new materials, it therefore becomes necessary to develop a method that can calculate the electrical properties without these assumptions.

The efforts toward such a goal have been evidenced by the development of density-functional perturbation theory (DFPT) [33] and the Wannier interpolation scheme [34], which allows the determination of the e-ph coupling matrix fully from first-principles calculations [35]. Restrepo *et al.* [36] presented the first *ab initio* mobility for the case of silicon. These techniques have since been widely used to investigate EPI and to compute thermoelectric properties [37–39] and electron mean free path (MFP) spectra [39] in silicon as well as the electrical resistivity in graphene [40–42] under RTA. Such density-functional-theory-based (DFT-based) treatment can also be employed to compute electron mobility in weakly polar materials such as transition metal dichalcogenides [43–46] and perovskites [47,48], in which RTA still works due to the suppression of LO-phonon scatterings by strong dielectric screening. For strongly polar materials, like GaAs, the long-range information originating from polar-optical-phonon and piezoelectric interactions in e-ph coupling matrices is lost during the Wannier interpolation [35]. The absence of such long-range contributions makes first-principles calculations of the scattering rate in polar semiconductors more challenging, until recently, when the "polar Wannier interpolation scheme" was proposed by Sjakste *et al.* [49], and by Verdi and Giustino [50], which adds in the long-range e-ph couplings. Despite these developments and the scattering rates obtained via such polar Wannier interpolation processes, efforts to compute electron transport properties such as mobility in polar materials by first-principle calculation are just beginning. In addition, the electron MFP spectra for polar semiconductors still remain unclear. The challenges result from, first, the necessity of a very fine sampling of the Brillouin zone to ensure the convergence of transport properties, which is extremely computationally demanding, and Second, the RTA, which is not well justified in polar materials; thus, the linearized BTE should be solved iteratively on a very fine mesh in order to determine the electron distribution function, rather than implementing RTA.

This paper conducts a detailed first-principles study of the electron transport properties in GaAs, a prototypical polar semiconductor with well-documented properties. The coupling matrices are computed via the polar Wannier interpolation scheme, and these are then used to obtain the electron scattering rates. The transport properties such as electron MFP are extracted from the exact solution of linearized BTE obtained by an iterative scheme. Although GaAs has been a

well-known material, our mode-by-mode analysis enables us to quantitatively determine the contributions of long-range and short-range scatterings as well as of intravalley and intervalley transitions in EPI, which shed light on the detailed scattering mechanisms that were previously lacking clarification till now. For example, we detail the trend of electron scattering rates especially close to the Γ point and the importance of piezoelectric interactions even at room temperature. The obtained spectral distribution of electron MFP is also useful when designing nanodevices using GaAs. More importantly, we expect this method to be applied to other materials to help understand their electron transport behavior.

II. METHODOLOGY

The key for studying electron transport is the determination of the e-ph coupling matrix within the first-principles framework, followed by the computation of the pursued transport property such as electron mobility by the exact solution of linearized e-ph BTE. The e-ph coupling matrix is given by [6]

$$\mathbf{M}_{n\mathbf{k},p\mathbf{q}}^{m\mathbf{k}+\mathbf{q}}=\left(\frac{\hbar}{2m_0\omega_{p\mathbf{q}}}\right)^{1/2}\langle m\mathbf{k}+\mathbf{q}|\delta V_{p\mathbf{q}}(\mathbf{r})|n\mathbf{k}\rangle, \quad (1)$$

where m_0 is a reference mass, $|n\mathbf{k}\rangle$ is the periodic part in the electron wave function $\psi_{n\mathbf{k}}(\mathbf{r})=\langle\mathbf{r}|n\mathbf{k}\rangle$, and $n\mathbf{k}$ and $p\mathbf{q}$ represent the wave vector for an electron at the n band and for a phonon at the p mode, respectively. δV_{pq} is the perturbed potential due to phonon vibration that can be computed by DFPT calculations. It should be emphasized that the DFPT calculations cannot yield a very precise value for the piezoelectric coefficient. For the III-V group semiconductors, the average calculation error of the first-order piezoelectric constant is 10% [51], and therefore approximately 20% error will be included in the piezoelectric interaction considering the coupling strength is measured proportionally to the square of the piezoelectric constant.

In this section, we will show the derivation for the linearized e-ph BTE and its exact solution solved by means of the iterative method. This solution, associated with the e-ph coupling matrix obtained by polar Wannier interpolation, will be used to compute the electron scattering rates as well as the transport properties. The simulation details and the convergence tests are also presented.

A. Iterative e-ph Boltzmann transport equation

The BTE describes the time evolution of a carrier's distribution. Diffusion in phase space as well as collision between carriers tend to deviate the distribution function from its equilibrium state. In the BTE approach, correlation between carriers is ignored—carriers are treated as particles for which MFPs should be much larger than the De Broglie wavelength [8]. Assuming the absence of temperature and electrochemical gradients, the BTE for a system at steady state can be written as [52]

$$\left(\frac{\partial f_{n\mathbf{k}}}{\partial t}\right)_{\mathrm{coll}}=-\left(\frac{\partial f_{n\mathbf{k}}}{\partial t}\right)_{\mathrm{diff}}. \quad (2)$$

In Eq. (2), the diffusion term on the right-hand side is given by $(\partial f_{n\mathbf{k}}/\partial t)_{\mathrm{diff}}=-e\mathbf{E}\cdot\mathbf{v}_{n\mathbf{k}}\partial f_{n\mathbf{k}}/\partial\varepsilon_{n\mathbf{k}}$, where $f_{n\mathbf{k}}$ is the distribution function of an electron in the nth band at wave vector $\mathbf{k}$. The electron energy and group velocity are represented by $\varepsilon_{n\mathbf{k}}$ and $\mathbf{v}_{n\mathbf{k}}$, respectively. $e\mathbf{E}$ is the electrical force acting on an electron. If we fix our attention to a specific state $n\mathbf{k}$, an electron can be scattered into/out of that state by absorbing/emitting a phonon of state $\pm p\mathbf{q}$. In this view, there are four mechanisms that should be taken into account in the three-carrier interaction. In terms of the first-order perturbation theory using Fermi's golden rule, the collision term in Eq. (2) can be evaluated by [52]

$$\left(\frac{\partial f_{n\mathbf{k}}}{\partial t}\right)_{\mathrm{coll}}=\frac{2\pi}{\hbar}\sum_{m\mathbf{k}+\mathbf{q}}|\mathbf{M}_{n\mathbf{k},p\mathbf{q}}^{m\mathbf{k}+\mathbf{q}}|^2\left\{\begin{bmatrix}\left(f_{n\mathbf{k}}^0+n_{-p\mathbf{q}}^0\right)f'_{m\mathbf{k}+\mathbf{q}}\\-\left(1+n_{-p\mathbf{q}}^0-f_{m\mathbf{k}+\mathbf{q}}^0\right)f'_{n\mathbf{k}}\end{bmatrix}\delta(\varepsilon_{n\mathbf{k}}-\varepsilon_{m\mathbf{k}+\mathbf{q}}-\hbar\omega_{-p\mathbf{q}})+\begin{bmatrix}\left(1-f_{n\mathbf{k}}^0+n_{p\mathbf{k}}^0\right)f'_{m\mathbf{k}+\mathbf{q}}\\-\left(n_{p\mathbf{q}}^0+f_{m\mathbf{k}+\mathbf{q}}^0\right)f'_{n\mathbf{k}}\end{bmatrix}\delta(\varepsilon_{n\mathbf{k}}+\hbar\omega_{p\mathbf{q}}-\varepsilon_{m\mathbf{k}+\mathbf{q}})\right\} \quad (3)$$

where $\hbar\omega_{p\mathbf{q}}$ is the energy of a phonon in the pth mode at wave vector $\mathbf{q}$. Equation (3) is derived based on the energy conservation conditions $(1-f_{n\mathbf{k}}^0)n_{-p\mathbf{q}}^0f_{m\mathbf{k}+\mathbf{q}}^0=f_{n\mathbf{k}}^0(1+n_{-p\mathbf{q}}^0)(1-f_{m\mathbf{k}+\mathbf{q}}^0)$ and $(1-f_{n\mathbf{q}}^0)(1+n_{p\mathbf{q}}^0)f_{m\mathbf{k}+\mathbf{q}}^0=f_{n\mathbf{k}}^0n_{p\mathbf{q}}^0(1-f_{m\mathbf{k}+\mathbf{q}}^0)$, and the electron distribution function is already written in terms of the deviation from the equilibrium distribution as $f_{n\mathbf{k}}=f_{n\mathbf{k}}^0+f'_{n\mathbf{k}}$. In this work, the phonons are always assumed to be at their equilibrium states, essentially neglecting the phonon drag effect, which mainly occurs at low temperature in semiconductors [53,54].

In the low-field transport regime, the deviation of the distribution function can be treated as a small perturbation from the equilibrium distribution. Based on this assumption, the diffusion term in Eq. (2) can then be rewritten as $(\partial f'_{n\mathbf{k}}/\partial t)_{\mathrm{diff}}=-e\mathbf{E}\cdot\mathbf{v}_{n\mathbf{k}}\partial f_{n\mathbf{k}}^0/\partial\varepsilon_{n\mathbf{k}}$. The single-mode RTA claims that $f'_{n\mathbf{k}}$ should vanish after a time period $\tau_{n\mathbf{k}}$, and thereby the deviation of the distribution function can be obtained explicitly, which reads $f'_{n\mathbf{k}}=e\mathbf{E}\cdot\mathbf{v}_{n\mathbf{k}}\tau_{n\mathbf{k}}\partial f_{n\mathbf{k}}^0/\partial\varepsilon_{n\mathbf{k}}$. Here, we can define an electron mean free displacement $\mathbf{F}_{n\mathbf{k}}\equiv\mathbf{v}_{n\mathbf{k}}\tau_{n\mathbf{k}}$, to be determined by iterative procedure as will be shown below, and the deviation of distribution function can be rewritten as

$$f'_{n\mathbf{k}}=-\frac{f_{n\mathbf{k}}^0\left(1-f_{n\mathbf{k}}^0\right)}{k_{\mathrm{B}}T}e\mathbf{E}\cdot\mathbf{F}_{n\mathbf{k}}. \quad (4)$$

We make use of Eq. (4) to linearize the collision integral in Eq. (3) and the diffusion term in Eq. (2). After equating Eqs. (2) and (3), the BTE is given by

$$\mathbf{v}_{n\mathbf{k}}=\sum_{m\mathbf{k}+\mathbf{q}}\left(\mathbf{G}_{n\mathbf{k}}^{m\mathbf{k}+\mathbf{q},-p\mathbf{q}}+\mathbf{G}_{n\mathbf{k},p\mathbf{q}}^{m\mathbf{k}+\mathbf{q}}\right)\left(\mathbf{F}_{n\mathbf{k}}-\mathbf{F}_{m\mathbf{k}+\mathbf{q}}\right), \quad (5)$$

where $\mathbf{G}_{n\mathbf{k}}^{m\mathbf{k+q},-p\mathbf{q}} = 2\pi/\hbar|\mathbf{M}_{n\mathbf{k},p\mathbf{q}}^{m\mathbf{k+q}}|^2(1+n_{-p\mathbf{q}}^0 - f_{m\mathbf{k+q}}^0)\delta(\varepsilon_{n\mathbf{k}} - \varepsilon_{m\mathbf{k+q}} - \hbar\omega_{-p\mathbf{q}})$ and $\mathbf{G}_{n\mathbf{k},p\mathbf{q}}^{m\mathbf{k+q}} = 2\pi/\hbar|\mathbf{M}_{n\mathbf{k},p\mathbf{q}}^{m\mathbf{k+q}}|^2(n_{p\mathbf{q}}^0 + f_{m\mathbf{k+q}}^0)\delta(\varepsilon_{n\mathbf{k}} + \hbar\omega_{p\mathbf{q}} - \varepsilon_{m\mathbf{k+q}})$ are the electron transition rates at equilibrium due to the phonon emission and absorption processes, respectively, which are computed by first-principles calculations in this work. Equation (5) can be further reorganized into an iterative form:

$$\mathbf{F}_{n\mathbf{k}}^{(i+1)} = \tau_{n\mathbf{k}}^{\mathrm{RTA}}\left[\mathbf{v}_{n\mathbf{k}} + \sum_{m\mathbf{k+q}}\left(\mathbf{G}_{n\mathbf{k}}^{m\mathbf{k+q},-p\mathbf{q}} + \mathbf{G}_{n\mathbf{k},\mathbf{kq}}^{m\mathbf{k+q}}\right)\mathbf{F}_{m\mathbf{k+q}}^{(i)}\right], \quad (6)$$

which is the so-called iterative e-ph BTE. Here, $\tau_{n\mathbf{k}}^{\mathrm{RTA}} = [\sum_{m\mathbf{k+q}}(\mathbf{G}_{n\mathbf{k}}^{m\mathbf{k+q},-p\mathbf{q}} + \mathbf{G}_{n\mathbf{k},p\mathbf{q}}^{m\mathbf{k+q}})]^{-1}$ is the relaxation time of an electron according to the Migdal approximation [55]. In this work, we deal with the surface integrals in the relaxation time by means of tetrahedral integration [56]. Once the relaxation time is determined, the mean free displacement $\mathbf{F}_{n\mathbf{k}}$ can therefore be solved iteratively. We straightforwardly set the initial $\mathbf{F}_{m\mathbf{k+q}}^{(0)}$ to be zero, thus leading to the MFP of an electron under RTA, $\mathbf{F}_{n\mathbf{k}}^{(1)} = \mathbf{v}_{n\mathbf{k}}\tau_{n\mathbf{k}}^{\mathrm{RTA}}$, as the first-order solution. Then, $\mathbf{F}_{m\mathbf{k+q}}^{(1)}$ can be obtained from $\mathbf{F}_{n\mathbf{k}}^{(1)}$ with a difference of phonon wave vector $\mathbf{q}$ to carry on the self-consistent calculations. The iteration procedure provides us with the true deviation of the electron distribution function given by Eq. (4) in the low-field transport limit for polar materials. Once the converged deviation function is achieved, the electron mobility tensor can be calculated by

$$\mu_{\alpha\beta} = \frac{2e}{\Omega N_{\mathbf{k}} n_c}\sum_{n\mathbf{k}} v_{n\mathbf{k},\alpha} F_{n\mathbf{k},\beta}\frac{\partial f_{n\mathbf{k}}^0}{\partial \varepsilon_{n\mathbf{k}}}, \quad (7)$$

where n_c is the carrier concentration, and $N_{\mathbf{k}}$ is the number of $\mathbf{k}$-point grids. The subscripts α and β denote the direction of electron transport.

B. Simulation details and convergence test

In the very first step, there are three physical quantities that should be determined: the electronic Hamiltonian, dynamical matrix, and phonon perturbation. These calculations are performed using the Quantum ESPRESSO package [57]. A Troullier-Martins norm-conserving pseudopotential with the Perdew-Wang exchange-correlation functional is employed to describe the interactions of Ga and As atoms. The cutoff energy of the plane wave is chosen as 80 Ry, and a $20 \times 20 \times 20$ mesh and a $6 \times 6 \times 6$ Monkhorst-Pack $\mathbf{k}$-point mesh are used for the self-consistent and non-self-consistent field calculations, respectively. The convergence threshold of energy is set to be 10^{-12} Ry. The obtained optimized lattice constant for GaAs is 5.53 Å. In the phonon calculations, the dynamical matrices and phonon perturbations are computed on a $6 \times 6 \times 6$ $\mathbf{q}$-point mesh. We suggest a threshold for phonon calculations to be 10^{-22} Ry to achieve better convergence of the phonon perturbation. We use the BerkeleyGW package [58] to produce a more accurate electron band structure. The cutoff energies of the screened and bare Coulomb potential are set by 15 and 45 Ry, respectively. In order to calculate the dielectric constant and Green's function, we must include 80 empty conduction bands in the calculation. The obtained bandgap is 1.411 eV, and the energy differences between Γ and L, and Γ and X valleys are 0.258 and 0.387 eV, respectively. The GW eigenvalues are computed on a $6 \times 6 \times 6$ $\mathbf{k}$-point mesh, with results used as the input in the subsequent calculations.

In this work, the EPW [59] package is employed to interpolate the e-ph coupling matrices as well as the electron and phonon eigenvalues from the coarse (obtained by DFT and DFPT calculations as mentioned) to fine $\mathbf{k}$- and $\mathbf{q}$-point meshes, using polar Wannier interpolation. Our in-house code, an iterative solver of the linearized e-ph BTE, is used to calculate the electron transport properties. Figures 1(a) and 1(b) show the convergence of electron mobility with respect to varying density of $\mathbf{q}$- and $\mathbf{k}$-point grids, respectively. We found that the calculation on a $600 \times 600 \times 600$ $\mathbf{k}$-point mesh associated with a $100 \times 100 \times 100$ $\mathbf{q}$-point mesh achieves the best balance between mobility convergence and computational efficiency. We thus use this optimized mesh throughout this work to compute transport properties. The mobility is considered as convergent while the variation is less than 0.1% as shown in the Fig. 1(c). The carrier concentration is taken to be 10^{13} cm^{-3} to characterize the Fermi level of an intrinsic GaAs. In this case, at 300 K, we find that the mobility has about an 18% increase compared to RTA's result once the convergence of the solution to e-ph BTE is achieved. Figure 1(d) demonstrates the electron scattering rates near the Γ point before (e.g., solely RTA implemented) and after iteration. The scattering rate in the iterative scheme is defined by the inverse of effective relaxation time, $\tau_{\mathrm{eff},n\mathbf{k}}^{-1} = (\mathbf{F}_{n\mathbf{k}} \cdot \mathbf{v}_{n\mathbf{k}}/|\mathbf{v}_{n\mathbf{k}}|^2)^{-1}$. The significant decrease in scattering rates compared to RTA shows the importance of solving the linearized BTE iteratively to more accurately study electron transport properties in polar materials.

C. Limitations of presented first-principles framework

In this work, we focus on phonon-induced electron transitions, and the formation of polaron is not involved. Although electron-electron (e-e) interactions, the phonon drag effect, and renormalization of electron effective mass due to the EPI are ignored, they will not affect the computed mobility too much due to their minor roles in electron transport in a nondegenerate semiconductor at room temperature. Explanations are provided as follows. (i) In the GW calculation, we found that the e-e self-energy is much smaller than the e-ph self-energy, which means that the electron transport is dominated by e-ph scatterings. A model study [60] also demonstrated that in intrinsic GaAs, including e-e scatterings will reduce mobility by 10% at 80 K, but the effect is negligible when the temperature is above 150 K. (ii) The phonon drag effect is only significant when the temperature is much lower than T_{D}, where T_{D} represents the Debye temperature and is around 360 K for GaAs. Moreover, the phonon drag effect influences the Seebeck coefficient much more than the mobility [54]. On the other hand, the assumption of equilibrium phonon distribution is used widely, in deriving phenomenological scattering models, as well as in other first-principles-based efforts [35,46], and in general, this assumption has been working well. (iii) Renormalization of the electron energy due to the EPI is usually much smaller than the dominant energy scale in our study, which is the energy bandgap. Experimental measurement [61] and first-principles calculation [62] found that the renormalization of the bandgap

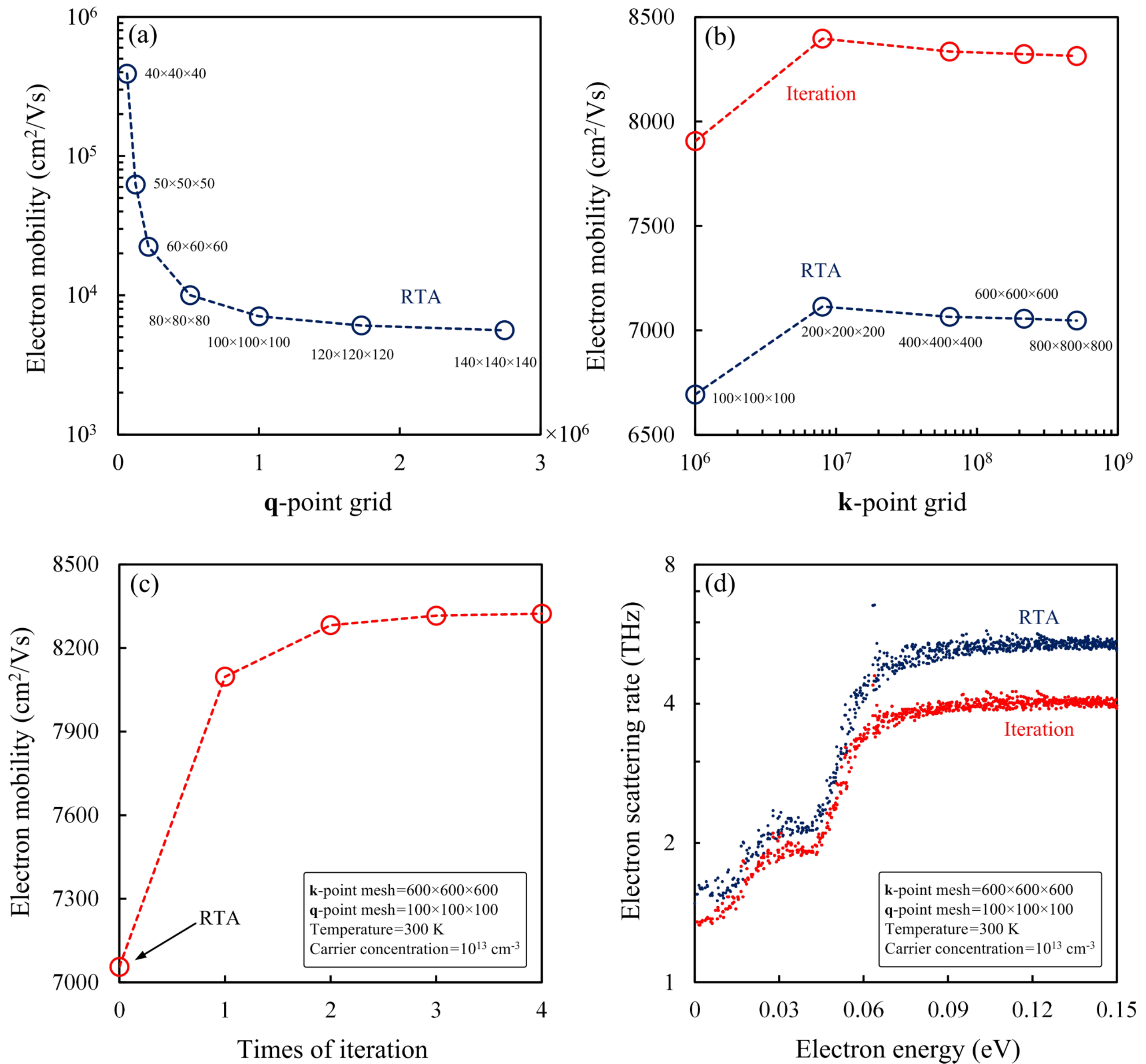

FIG. 1. (a) Electron mobility computed by a fixed $600 \times 600 \times 600$ **k**-point mesh with respect to varying density of **q**-point grids. (b) Electron mobility computed by a fixed $100 \times 100 \times 100$ **q**-point mesh with respect to varying density of **k**-point grids. The blue and red circles are the mobilities calculated from the RTA and iterative scheme, respectively. (c) Evolution of electron mobility with respect to times of iteration. (d) Electron scattering rates near the Γ point. The blue and red dots are the scattering rates computed by using the RTA and iterative scheme, respectively, from the $600 \times 600 \times 600$ **k**-point and $100 \times 100 \times 100$ **q**-point meshes. The studied temperature and carrier concentration in these simulations as shown in the four panels are 300 K and 10^{13} cm^{-3}, respectively.

in GaAs is only about 0.04 eV. We also note that without considering this electron energy renormalization mediated by EPI, researchers have shown reasonable electron scattering rates for GaAs [49] and TiO_2 [50], and therefore our treatment here by ignoring the electron renormalization due to e-ph interaction should be good enough for the transport properties, which is also confirmed by the calculated mobility compared with experiments.

III. RESULTS AND DISCUSSION

In Fig. 2, we demonstrate the capability of using first-principles calculations to obtain electron scattering rates in GaAs. Figure 2(a) shows the energy-dependent scattering rate within 0.5 eV of the conduction band edge. By comparing the first-principles results with the semiempirical model, several significant differences can be seen. Our simulation shows that the scattering rate has a jump very close to the Γ point, which is due to the contribution of longitudinal-acoustic-phonon (LA-phonon) and transverse-acoustic-phonon (TA-phonon) scatterings, whereas the model largely underestimates the scatterings of acoustic phonons near the Γ point, and as a result, the trend is still inaccurately determined by the LO phonons. Furthermore, when the energy increases following onset of phonon emission processes participating in EPI, the computed scattering rate shows a slightly increasing trend

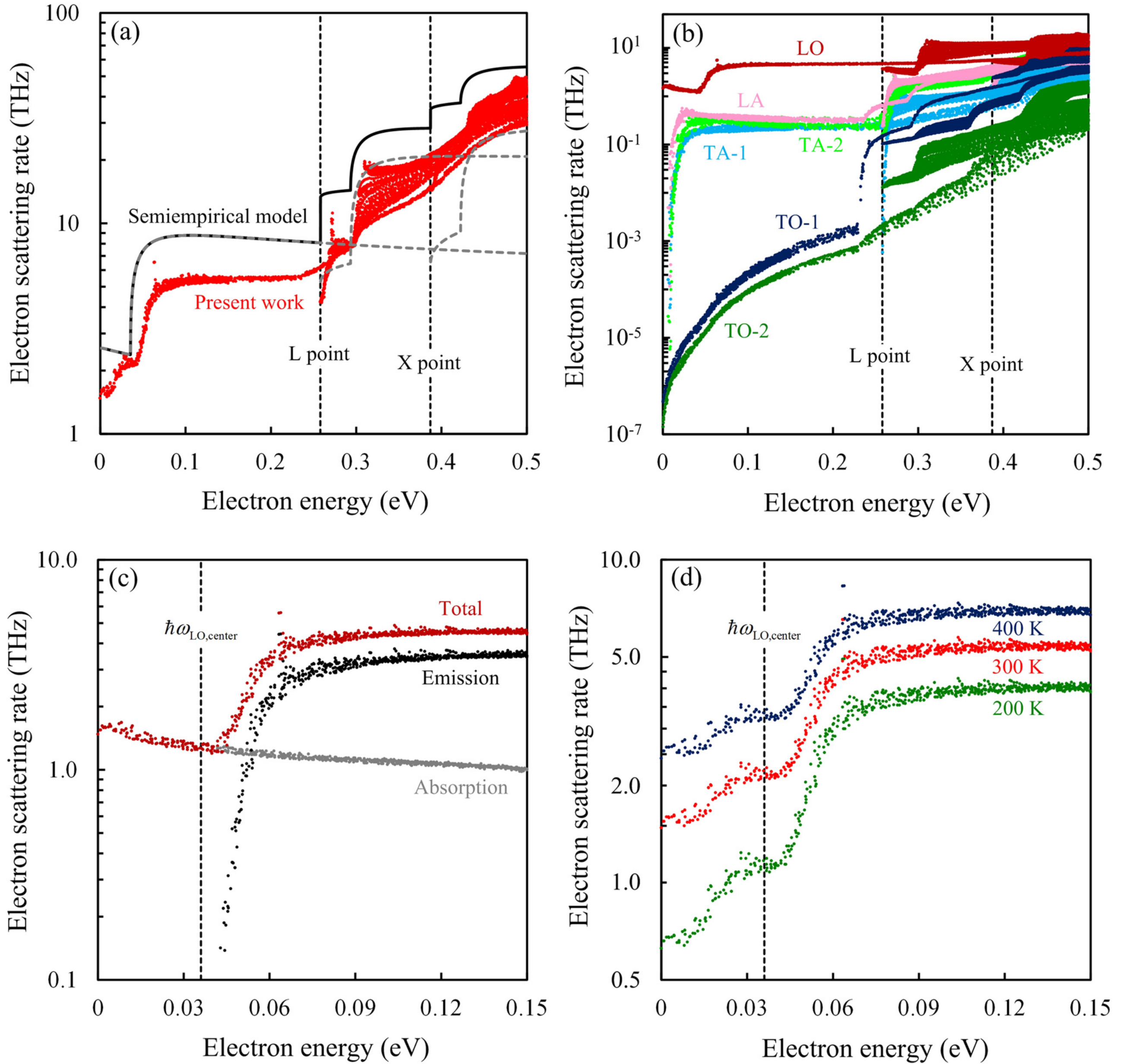

FIG. 2. (a) Electron scattering rate with respect to different electron energies at 300 K. The red dots are computed by present first-principles calculations. The black (total) and gray-dash (each valley) lines are predicted by the semiempirical models including acoustic-deformation-potential, piezoelectric, and polar-optical-phonon scatterings, which are listed in Table I. The parameters in these formulae are provided in Ref. [8]. (b) Electron scattering rate with respect to different electron energies due to each phonon mode at 300 K. (c) LO-phonon-limited electron scattering rate near the Γ point at 300 K. The black and gray dots are the scattering rates due to LO-phonon emission and absorption processes, respectively. The dark-red dots represent the total scattering. (d) Electron scattering rate near the Γ point at 200, 300, and 400 K, represented by green, red, and blue dots, respectively.

versus energy at the Γ valley that is in contrast with the model's prediction, which can be attributed to the nonparabolicity of the conduction band of GaAs as was discussed before [8]. In the higher-energy valleys, the models reveal surprisingly significant inconsistencies compared to first-principles calculations, particularly at the X valley. These discrepancies mainly come from the lack of consideration of the intervalley scattering in the semiempirical model [8]. Overall, the mobility evaluated through semiempirical modeling is $4930\,\mathrm{cm}^2/\mathrm{Vs}$ at 300 K, while the first-principles calculation presents a more reasonable value of $7050\,\mathrm{cm}^2/\mathrm{Vs}$ under RTA. These two effects—non-parabolicity of the conduction band and intervalley scattering—are automatically included in the first-principles calculation, but they are difficult to incorporate otherwise, especially when modeling complex band structures.

With the first-principles approach, as displayed in Fig. 2(b), we can now look at the contribution by EPI from each phonon mode with respect to different energies and valleys. For polar materials, the majority of momentum change of electrons results from the scattering by LO phonons, which has been

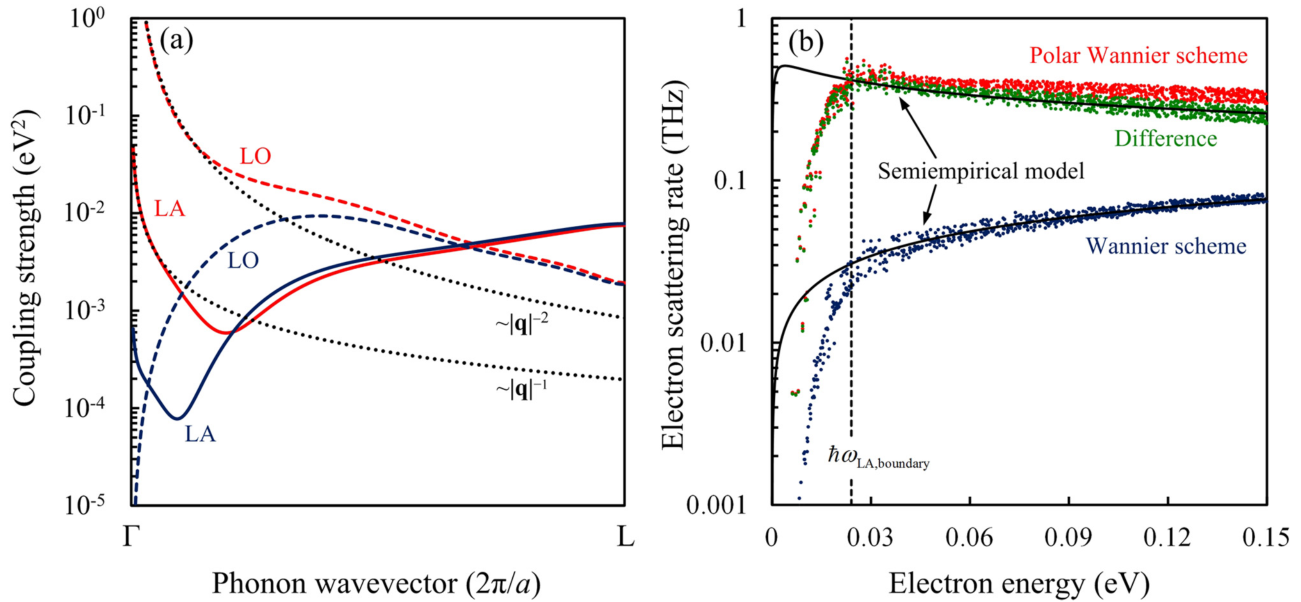

FIG. 3. (a) First-principles coupling strength $|\mathbf{M}_\mathbf{q}|^2$ between electrons at the Γ point and different phonons in the direction from Γ to L points. Red and blue colors denote the use of polar Wannier and Wannier interpolation schemes, respectively. The solid lines are LA phonons, and dashed lines are LO phonons. The black-dotted lines show the $\mathbf{q}$ dependencies on coupling strength: $|\mathbf{M}_\mathbf{q}^{\mathrm{PZ}}|^2 \sim |\mathbf{q}|^{-1}$ and $|\mathbf{M}_\mathbf{q}^{\mathrm{POP}}|^2 \sim |\mathbf{q}|^{-2}$. (b) Electron scattering rates due to LA phonons near the Γ point at 300 K. The red and blue dots are computed by using the polar Wannier scheme and Wannier scheme, respectively. The green dots are the difference in scattering rate between the two interpolated schemes. The upper and lower black lines display the trend of scattering rate versus energy of piezoelectric and acoustic-deformation-potential scatterings. It should be emphasized that because the semiempirical models largely underestimate the acoustic-phonon scattering rates in GaAs, particularly near the Γ point, we have adjusted the prefactors of piezoelectric and acoustic-deformation-potential scatterings listed in Table I to fit the simulation results in order to show a better comparison.

widely studied in the literature [6–8]. It also offers us a route to examine the detailed EPIs due to phonon absorption and emission processes mode-by-mode as shown in Fig. 2(c). The electron-LO-phonon interaction in a semiconductor is dominated by the absorption process when the electron energy is smaller than the LO-phonon energy at the Brillouin zone center, $\hbar\omega_{\mathrm{LO,center}}$. Then, the LO-phonon emission process takes over the EPI as the electron energy increases. The scattering rates computed at 200, 300, and 400 K are shown in Fig. 2(d). We can see the scattering rates shift upward while the temperature increases due to the increased phonon population of each mode under the RTA (phonons are kept in their equilibrium states), consistent with theoretical prediction [63].

When we examine the e-ph coupling strength as displayed in Fig 3(a), except for the case of the LO phonon, which has been discussed before [49,50], it is found that the LA-phonon coupling strength $|\mathbf{M}_\mathbf{q}|^2$ also exhibits a remarkable increase after the polar Wannier interpolation scheme is applied. The obtained trend of coupling strength at long-wavelength phonon wave vectors is proportional to $|\mathbf{q}|^{-1}$, which is in accordance with the semiempirical model for piezoelectric interactions as listed in Table I. This observation can be attributed to the fact that most of the long-range piezoelectric interactions are lost during the conventional interpolated procedure, whereas these interactions can be preserved during the polar Wannier interpolation. Furthermore, this also implies that the LA-phonon scattering rate might be largely underestimated in GaAs when the contribution of piezoelectric interaction is simply neglected. Figure 3(a) shows the electron scattering rates due to LA phonons calculated by using polar Wannier and Wannier interpolation, along with the differences between the two schemes. Generally, for the acoustic mode, one obtains $\varepsilon^{0.5}$ energy dependence for the scattering rate from deformation-potential scattering, and this is well captured by Wannier interpolation. However, the calculation results obtained through the polar Wannier interpolation indicate that the energy dependence of LA-phonon scatterings is much different from that of the deformation-potential scattering. The scattering rates have at least a twofold increase within the studied energy region. By comparing the scattering rate between the two methods, we find that their difference can be well fitted by the typical trend of piezoelectric scattering as shown in Table I. A theoretical study presented by Wolfe *et al.* [64] shows that in GaAs, the piezoelectric scattering is comparable to the deformation-potential scattering only when the temperature is lower than 100 K. However, our first-principles results indicate that the piezoelectric interaction dominates the electron-acoustic-phonon interaction in GaAs even at room temperature. Such EPI is inherently taken into account in DFPT (linear-response theory) calculations, which have been employed to compute the proper piezoelectric tensor [51,65]. Although DFPT can only provide the first-order contribution to the piezoelectric field, recent experimental and theoretical studies [66,67] show that the second-order effect in $In_xGa_{1-x}As$ is safely negligible when the concentration of In atoms is low, that is, when the lattice strain is very small. It is worth noting that for both piezoelectric and deformation-potential scattering, the trends

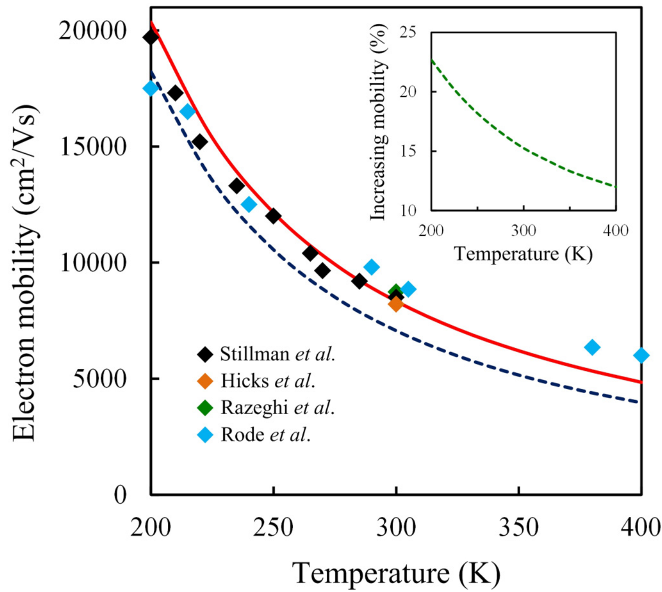

FIG. 4. Electron mobility with respect to temperature from 200 to 400 K. The red and blue dashed lines are the first-principles mobilities computed by the iterative scheme and RTA, respectively. The colored diamonds are the experimental measurements of the intrinsic GaAs [24,68–70]. The green dashed line in the inset represents the increase of mobility once the LA-phonon scattering is artificially removed.

fitted by models show remarkable inconsistencies with the first-principles results in GaAs, when the energy is lower than the LA-phonon energy at the zone boundary, $\hbar\omega_{\mathrm{LA,boundary}}$. This is because the models are derived based on the elastic assumption, which treats the phonon absorption and emission in the same way, and therefore they cannot well characterize the scattering rate for emission processes at the bottom of the valley.

Next, we proceed to discuss the electron transport properties. The scattering rates displayed in Figs. 2 and 3 are computed based on the RTA. These, however, cannot be directly used to evaluate the transport properties in polar materials. Instead, the fully iterative scheme for the linearized e-ph BTE should be applied to correctly determine the deviation of the distribution function from Eq. (4). This is expected to be particularly important for high-mobility materials, in which electron transport is often dominated by long-range polar interaction. As displayed in Fig. 4, our calculation results are in good agreement with experimental measurements in a temperature range of 200 to 400 K [24,68–70]; the computed electron mobility at 300 K is $8340\,\mathrm{cm}^2/\mathrm{Vs}$. The mobilities obtained from the iterative method are always larger than those from the RTA in the temperature range we studied, as indicated by the blue-dashed line in Fig. 4. There are two perspectives on why RTA underestimates mobility in polar materials. One is due to the phonon energy—the LO phonon has a nonnegligible energy compared with electrons that are close to the conduction band edge, and as a consequence, the electron-LO-phonon scattering cannot be considered as an elastic process [8]. An alternative perspective focuses on the magnitude of the electron-LO-phonon coupling strength. The probability of an electron interacting with an LO phonon with long wavelength is so high (see $\mathbf{M}_{\mathbf{q}}^{\mathrm{POP}}$ in Table I) that the distribution of the scattered electron can no longer be treated as close to the equilibrium state as claimed by the RTA [7]. Both perspectives point out a relevant fact; in such cases, a relaxation time cannot be defined. Our simulations show that at very low temperatures, there is no change in electron mobility following iteration since the LO phonons are not populated. As temperature increases, the electron-LO-phonon scattering starts to take over normal EPI, and as a result, the deviation of the distribution function of scattered electrons becomes larger. The calculation shows that at 200, 300, and 400 K, the iteration scheme provides 11%, 18%, and 22% correction to mobility, respectively, compared with RTA, which mainly results from accumulated deviation of the electron distribution function due to the strong coupling between electrons and long-wavelength phonons. The first-principles calculations can be used to more precisely quantify the effect of scattering from different phonon modes on electron transport. We have shown above that for the LA phonon, both piezoelectric and deformation-potential scatterings contribute to EPI near room temperature. Here, we further show that it has a nonnegligible effect on electron transport, as displayed by the green dashed line in the inset in Fig. 4. The mobility increases by 23% to 12% when the temperature varies from 200 to 400 K, if we artificially exclude the electron-LA-phonon interactions. The trend also indicates that the acoustic-phonon scatterings become dominant at low temperatures, which is in accordance with predictions from piezoelectric and deformation-potential theory.

Now we discuss another important property, the electron MFP. The mean free displacement $\mathbf{F}_{n\mathbf{k}}$ shown in Eq. (6) cannot characterize the MFP of an electron at eigenstate $n\mathbf{k}$ (unless we equate all $\mathbf{F}_{m\mathbf{k}+\mathbf{q}}$ to zero), due to the fact that it is mixed with other eigenstates $m\mathbf{k}+\mathbf{q}$ after iteration. Although the direction of the mean free displacement is no longer identical to that of energy flow, we can define an effective scalar MFP by projecting $\mathbf{F}_{n\mathbf{k}}$ onto its group velocity as $\Lambda_{n\mathbf{k}} = \mathbf{F}_{n\mathbf{k}} \cdot \mathbf{v}_{n\mathbf{k}}/|\mathbf{v}_{n\mathbf{k}}|$ [71]. The MFP spectrum at different temperatures as shown in Fig. 5(a) is a crucial quantity in engineering or designing nanostructures for various devices, but for GaAs and other polar semiconductors, it still remains unclear. The electron MFP of GaAs characterized by the Drude model is about 35 nm, which is obviously too small, since the free electron approximation is unable to reflect the correct picture of an electron moving in a periodic potential. The presented MFP spectra show that electrons that contribute to the mobility have a narrow span of MFP, between 130 and 210 nm at 300 K. It also shows that the MFP spectrum becomes wider at lower temperatures, since the dominant electron-LO-phonon scattering rate drops rapidly with a decrease in temperature, giving rise to an overall increase in the MFPs. The distribution of the MFP with respect to varying electron energy is demonstrated in Fig. 5(b). By comparing Figs. 5(a) and (b), we can determine the energy range that contributes most to the mobility in nanostructures. In polar materials, Howarth and Sondheimer [19] proposed that the MFP, as a function of energy and temperature, should be proportional to εT^{-1}. The first-principles MFPs show agreement with the trend after the phonon emission process fully takes over the EPI

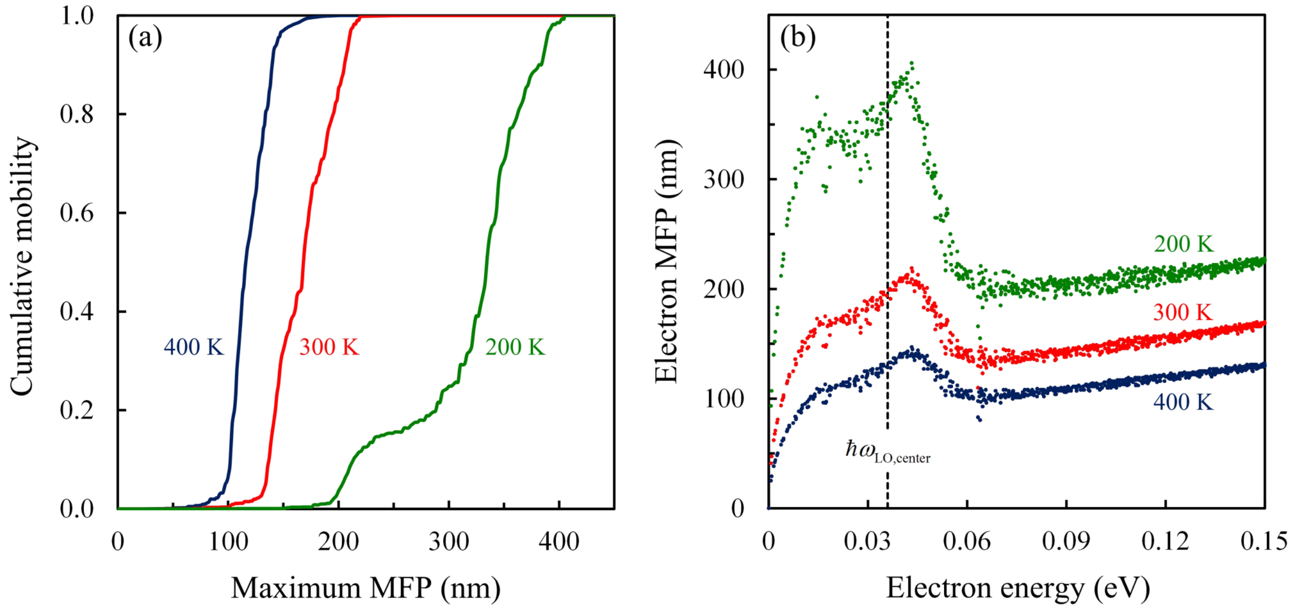

FIG. 5. (a) Cumulative mobilities with respect to different maximum MFPs of GaAs at 200, 300, and 400 K, represented by green, red, and blue lines, respectively. The electron MFP spectrum has been normalized by $\mu(\Lambda_{max})$ for each temperature. (b) Electron MFPs near the Γ point at 200, 300, and 400 K, represented by green, red, and blue lines, respectively.

(approximately when $\varepsilon_{n\mathbf{k}}$ is greater than 0.06 eV). However, near the conduction band edge, we can see the MFP has a local maximum that takes place around the energy of $\hbar\omega_{LO,center}$, since only the phonon absorption process has a substantial contribution to the EPI, and then it goes to zero as the group velocity is zero at the bottom of the valley.

Finally, we want to discuss the electron's intravalley and intervalley transitions at the L and X points, which reveal crucial information for understanding hot electron thermalization processes, and which are of great value in studying III-V semiconductor devices. The intervalley transitions due to deformation-potential scatterings in GaAs and other zinc-blende crystals have been studied by Zollner *et al.* [72,73]. Figure 6 shows the electron transition rates in a color map at each participation phonon mode, where the completed EPIs have been taken into account in the first-principles calculation automatically. We display the possible transition events of the EPI at the L and X points, and the dark-blue region means no scattering can be induced by these phonons. We do not show the case at the Γ point, because most of the scatterings at the Γ point are induced by small wave vector LO phonons due to its isolation from the other two valleys; the energy differences between the Γ and L points and between the Γ and X points are about 0.258 and 0.387 eV, respectively. This indicates that EPIs are dominated by the electron-LO-phonon scatterings, and that the excited electron near the Γ point will thermalize towards the conduction band edge mainly by emitting long-wavelength LO phonons. On the contrary, the intervalley transitions have substantial contributions to EPI at the L and X points. In the case of electrons at the L and X points, we can see distinct regions where the transition usually happens, which can be denoted by the three characteristic phonon wave vectors: $\mathbf{q} < 0.30$ (intravalley), $\mathbf{q} \sim 0.87$ (intervalley), and $\mathbf{q} \sim 1.00$ (intervalley). For the L point, $\mathbf{q} \sim 0.87$ represents the intervalley transition from the L point to the Γ and X valleys, and $\mathbf{q} \sim 1.00$ represents the intervalley transition from the L point to the other degenerate L valleys. On the other hand, at the X point, $\mathbf{q} \sim 0.87$ represents the transition from the X point to the L valley, and $\mathbf{q} \sim 1.00$ represents the intervalley transition from the X point to the Γ valley and to other degenerate X valleys. Our calculations indicate that the intervalley transitions contribute 13.2% and 57.6% to the total scattering rate of electrons at the L and X points, respectively. On the other hand, the contribution from acoustic phonons in EPI is 10.7% and 51.2% at the L and X points, respectively. These facts demonstrate that at the X point, the electron scattering is dominated by the intervalley transitions,

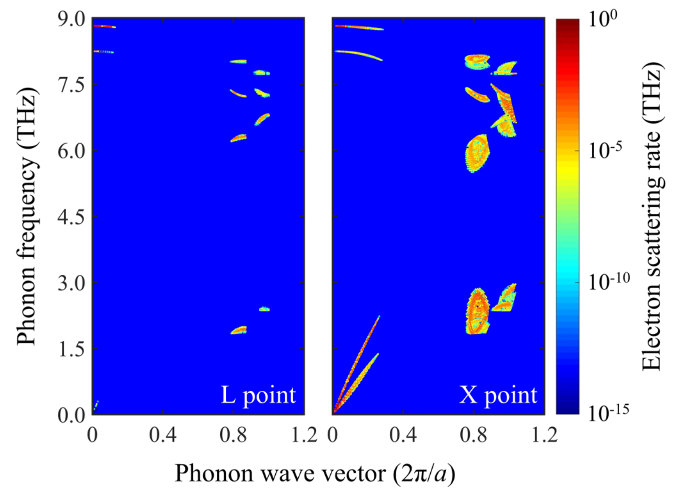

FIG. 6. The electron scattering rates at the L (left) and X (right) points due to phonons at 300 K in the entire Brillouin zone, plotted using absolute values of the phonon wave vector.

and the contribution from acoustic phonons, particularly the LA mode, in EPI cannot be simply neglected.

IV. CONCLUSION

In summary, we present a parameter-free first-principles framework to study EPI in GaAs. This general computational scheme further enables us to examine the details of each scattering event, which happens, particularly, around the bottom of the valleys. The computed electron mobilities are in good agreement with experimental results; however, detailed scattering mechanisms differ from semiempirical models, which are derived based upon many assumptions. Furthermore, the mode-by-mode analysis enables us to identify three features: (i) We identify the importance of piezoelectric scatterings in polar materials. The scattering rates of LA phonons show at least a twofold increase when the long-range piezoelectric interaction can be well addressed by the polar Wannier scheme. Both the piezoelectric and deformation-potential scatterings of LA phonons have nonnegligible contributions to EPI even at room temperature; they account for 15% reduction of the mobility at 300 K, and their presence changes the energy dependency of the scattering rate near the band edge. (ii) We identify the spectral distribution of the electron MFP. The main contributions to mobility are from electrons with MFPs between 130 and 210 nm at room temperature. The MFPs near the Γ point are also presented, which is hard to predict by the proposed model. (iii) We identify the quantitative determination of intravalley and intervalley transitions. At the X point, the intervalley transitions provide 57.6% of the total e-ph scatterings, which is comparable to the intravalley transitions. We also identify that 51.2% of scattering is contributed by acoustic phonons. Thus, detailed information about specific channels for e-ph scattering can be obtained and used in designing materials as well as devices where phonon scattering, including polar optical phonon scattering, controls the mobility. We expect the presented general framework can be applied to other structures and facilitate the understanding of electron transport in new materials.

Note added. Very recently, Zhou and Bernardi reported a related first-principles calculation of electron mobility in GaAs based on RTA [74]. According to their "Note added", their work has improved, particularly, the convergence with respect to **k**- and **q**-point meshes and the smearing technique used in the calculations. The number of **q**-point meshes, as they point out, will critically affect the computed mobility. In this work, we used a similar mesh density associated with tetrahedral smearing in evaluating the electron relaxation time, but we solved the linearized e-ph BTE instead of using RTA. We found that regardless of the mesh density used, the mobility obtained using RTA is underestimated compared to the full solution from linearized e-ph BTE, which also agrees with previous work using empirical scattering models [22–25]. This indicates that obtaining the full solution from the BTE is important for polar materials like GaAs, which is also discussed in Fig. 4.

ACKNOWLEDGMENTS

We thank Laureen Meroueh, Wei-Chun Hsu, Qichen Song, and Zhiwei Ding for helpful discussions. This article was supported by S[3]TEC, an Energy Frontier Research Center funded by the U.S. Department of Energy, Office of Basic Energy Sciences, under Award DE-FG02-09ER46577 (for fundamental research on electron-phonon interaction in thermoelectric materials) and by the DARPA MATRIX program, under Grant HR0011-16-2-0041 (for developing and applying the simulation codes).

Te-Huan Liu and Jiawei Zhou contributed equally to this work.

[1] F. Bloch, Z. Phys. **52**, 555 (1928).
[2] J. Bardeen and D. Pines, Phys. Rev. **99**, 1140 (1955).
[3] G. Grimvall, *The Electron-Phonon Interaction in Metals* (North Holland Publishing Company, Amsterdam, 1981).
[4] J. Bardeen and W. Shockley, Phys. Rev. **80**, 72 (1950).
[5] C. Herring and E. Vogt, Phys. Rev. **101**, 944 (1956).
[6] J. M. Ziman, *Electrons, and Phonons: The Theory of Transport Phenomena in Solids* (Clarendon Press, Oxford, 1960).
[7] K. Hess, *Advanced Theory of Semiconductor Devices* (Wiley-IEEE Press, Piscataway, NJ, 1999).
[8] M. Lundstrom, *Fundamentals of Carrier Transport* (Cambridge University Press, Cambridge, UK, 2009).
[9] H. Fröhlich, Proc. Roy. Soc. A **188**, 521 (1947).
[10] E. J. Ryder, Phys. Rev. **90**, 766 (1953).
[11] J. Bardeen, L. N. Cooper, and J. R. Schrieffer, Phys. Rev. **108**, 1175 (1957).
[12] D. Pines, Phys. Rev. **109**, 280 (1958).
[13] W. A. Harrison, Phys. Rev. **104**, 1281 (1956).
[14] W. Pötz and P. Vogl, Phys. Rev. B **24**, 2025 (1981).
[15] H. J. G. Meijer and D. Polder, Physica **19**, 255 (1953).
[16] H. Fröhlich, Adv. Phys. **3**, 325 (1954).
[17] P. Vogl, Phys. Rev. B **13**, 694 (1976).
[18] A. R. Hutson, J. Appl. Phys. **32**, 2287 (1961).
[19] D. J. Howarth, and E. H. Sondheimer, Proc. Roy. Soc. A-Math. Phys. Eng. Sci. **219**, 53 (1953).
[20] H. Ehrenreich, Phys. Rev. **120**, 1951 (1960).
[21] H. Ehrenreich, J. Appl. Phys. **32**, 2155 (1961).
[22] D. L. Rode, Phys. Rev. B **2**, 1012 (1970).
[23] D. L. Rode, Phys. Rev. B **2**, 4036 (1970).
[24] D. L. Rode and S. Knight, Phys. Rev. B **3**, 2534 (1971).
[25] D. L. Rode, Phys. Rev. B **3**, 3287 (1971).
[26] S. Dhar and S. Ghosh, J. Appl. Phys. **86**, 2668 (1999).
[27] A. T. Ramu, L. E. Cassels, N. H. Hackman, H. Lu, J. M. O. Zide, and J. E. Bowers, J. Appl. Phys. **107**, 083707 (2010).
[28] A. Faghaninia, J. W. Ager III, and C. S. Lo, Phys. Rev. B **91**, 235123 (2015).
[29] M. V. Fischetti and S. E. Laux, Phys. Rev. B **38**, 9721 (1988).
[30] M. V. Fischetti and S. E. Laux, Phys. Rev. B **48**, 2244 (1993).
[31] M. V. Fischetti and S. E. Laux, J. Appl. Phys. **80**, 2234 (1996).
[32] B. K. Ridley, *Quantum Processes in Semiconductors* (Oxford University Press, New York, 2000).
[33] S. Baroni, S. de Gironcoli, A. D. Corso, and P. Giannozzi, Rev. Mod. Phys. **73**, 515 (2001).

[34] N. Marzari, A. A. Mostofi, J. R. Yates, I. Souza, and D. Vanderbilt, Rev. Mod. Phys. **84**, 1419 (2012).
[35] F. Giustino, M. L. Cohen, and S. G. Louie, Phys. Rev. B **76**, 165108 (2007).
[36] O. D. Restrepo, K. Varga, and S. T. Pantelides, Appl. Phys. Lett. **94**, 212103 (2009).
[37] Z. Wang, S. Wang, S. Obukhov, N. Vast, J. Sjakste, V. Tyuterev, and N. Mingo, Phys. Rev. B **83**, 205208 (2011).
[38] B. Liao, B. Qiu, J. Zhou, S. Huberman, K. Esfarjani, and G. Chen, Phys. Rev. Lett. **114**, 115901 (2015).
[39] B. Qiu, Z. Tian, A. Vallabhaneni, B. Liao, J. M. Mendoza, O. D. Restrepo, X. Ruan, and G. Chen, Europhys. Lett. **109**, 57006 (2015).
[40] K. M. Borysenko, J. T. Mullen, E. A. Barry, S. Paul, Y. G. Semenov, J. M. Zavada, M. Buongiorno Nardelli, and K. W. Kim, Phys. Rev. B **81**, 121412 (2010).
[41] T. Sohier, M. Calandra, C.-H. Park, N. Bonini, N. Marzari, and F. Mauri, Phys. Rev. B **90**, 125414 (2014).
[42] C. H. Park, N. Bonini, T. Sohier, G. Samsonidze, B. Kozinsky, M. Calandra, F. Mauri, and N. Marzari, Nano Lett. **14**, 1113 (2014).
[43] X. Li, J. T. Mullen, Z. Jin, K. M. Borysenko, M. B. Nardelli, and K. W. Kim, Phys. Rev. B, **87**, 115418 (2013).
[44] O. D. Restrepo, K. E. Krymowski, J. Goldberger, and W. Windl, New J. Phys. **16**, 105009 (2014).
[45] T. Gunst, T. Markussen, K. Stokbro, and M. Brandbyge, Phys. Rev. B **93**, 035414 (2016).
[46] W. Li, Phys. Rev. B **92**, 075405 (2015).
[47] B. Himmetoglu, A. Janotti, H. Peelaers, A. Alkauskas, and C. G. Van de Walle, Phys. Rev. B **90**, 241204 (2014).
[48] B. Himmetoglu and A. Janotti, J. Phys.: Condens. Matter **28**, 065502 (2016).
[49] J. Sjakste, N. Vast, M. Calandra, and F. Mauri, Phys. Rev. B **92**, 054307 (2015).
[50] C. Verdi, and F. Giustino, Phys. Rev. Lett. **115**, 176401 (2015).
[51] S. de Gironcoli, S. Baroni, and R. Resta, Phys. Rev. Lett. **62**, 2853 (1989).
[52] G. Chen, *Nanoscale Energy Transport, and Conversion: A Parallel Treatment of Electrons, Molecules, Phonons, and Photons* (Oxford University Press, New York, 2005).
[53] C. Herring, Phys. Rev. **96**, 1163 (1954).
[54] J. Zhou, B. Liao, B. Qiu, S. Huberman, K. Esfarjani, M. S. Dresselhaus, and G. Chen, Proc. Natl. Acad. Sci. U.S.A. **112**, 14777 (2015).
[55] A. B. Migdal, Zh. Eksp. Teor. Fiz. **34**, 1438 (1958) [Sov. Phys. JETP **34**, 996 (1958)].
[56] P. Lambin and J. P. Vigneron, Phys. Rev. B **29**, 3430 (1984).
[57] P. Giannozzi, S. Baroni, N. Bonini, M. Calandra, R. Car, C. Cavazzoni, D. Ceresoli, G. L. Chiarotti, M. Cococcioni, I. Dabo, A. Dal Corso, S. Fabris, G. Fratesi, S. de Gironcoli, R. Gebauer, U. Gerstmann, C. Gougoussis, A. Kokalj, M. Lazzeri, L. Martin-Samos, N. Marzari, F. Mauri, R. Mazzarello, S. Paolini, A. Pasquarello, L. Paulatto, C. Sbraccia, S. Scandolo, G. Sclauzero, A. P. Seitsonen, A. Smogunov, P. Umari, and R. M. Wentzcovitch, J. Phys.: Condens. Matter **21**, 395502 (2009).
[58] J. Deslippe, G. Samsonidze, D. A. Strubbe, M. Jain, M. L. Cohen, and S. G. Louie, Comput. Phys. Commun. **183**, 1269 (2012).
[59] S. Poncé, E. R. Margine, C. Verdi, and F. Giustino, Comput. Phys. Commun. **209**, 116 (2016).
[60] D. Chattopadhyay, J. Appl. Phys. **53**, 3330 (1982).
[61] E. Grilli, M. Guzzi, R. Zamboni, and L. Pavesi, Phys. Rev. B **45**, 1638 (1992).
[62] D. Olguín, M. Cardona, and A. Cantarero, Solid State Commun. **122**, 575 (2002).
[63] B. A. Mason and S. D. Sarma, Phys. Rev. B **35**, 3890 (1987).
[64] C. M. Wolfe, G. E. Stillman, and W. T. Lindley, J. Appl. Phys. **41**, 3088 (1970).
[65] M. N. Blonsky, H. L. Zhuang, A. K. Singh, and R. G. Hennig, ACS Nano **9**, 9885 (2015).
[66] G. Bester, X. Wu, D. Vanderbilt, and A. Zunger, Phys. Rev. Lett. **96**, 187602 (2006).
[67] M. A. Migliorato, D. Powell, A. G. Cullis, T. Hammerschmidt, and G. P. Srivastava, Phys. Rev. B **74**, 245332 (2006).
[68] H. G. B. Hicks and D. F. Manley, Solid State Commun. **7**, 1463 (1969).
[69] G. E. Stillman, C. M. Wolfe, and J. Dimmock, J. Phys. Chem. Solids **31**, 1199 (1970).
[70] M. Razeghi, F. Omnes, J. Nagle, M. Defour, O. Acher, and P. Bove, Appl. Phys. Lett. **55**, 1677 (1989).
[71] W. Li, J. Carrete, N. A. Katcho, and N. Mingo, Comp. Phys. Commun. **185**, 1747 (2014).
[72] S. Zollner, S. Gopalan, and M. Cardona, Appl. Phys. Lett. **54**, 614 (1989).
[73] S. Zollner, S. Gopalan, and M. Cardona, J. Appl. Phys. **68**, 1682 (1990).
[74] J. J. Zhou, and M. Bernardi, Phys. Rev. B **94**, 201201(R) (2016).